Antiferromagnetic Spinor Condensates in a Two-Dimensional Optical Lattice

L. Zhao, J. Jiang, T. Tang, M. Webb, and Y. Liu*
Department of Physics, Oklahoma State University, Stillwater, Oklahoma 74078, USA
(Received 30 December 2014; published 4 June 2015)

We experimentally demonstrate that spin dynamics and the phase diagram of spinor condensates can be conveniently tuned by a two-dimensional optical lattice. Spin population oscillations and a lattice-tuned separatrix in phase space are observed in every lattice where a substantial superfluid fraction exists. In a sufficiently deep lattice, we observe a phase transition from a longitudinal polar phase to a broken-axisymmetry phase in steady states of lattice-confined spinor condensates. The steady states are found to depend sigmoidally on the lattice depth and exponentially on the magnetic field. We also introduce a phenomenological model that semiquantitatively describes our data without adjustable parameters.

DOI: 10.1103/PhysRevLett.114.225302 PACS numbers: 67.85.Fg, 03.75.Kk, 03.75.Mn, 05.30.Rt

A spinor Bose-Einstein condensate (BEC) confined in optical lattices has attracted much attention for its abilities to systematically study, verify, and optimize condensed matter models [1–3]. An optical lattice is a versatile technique to enhance interatomic interactions and control the mobility of atoms [4–6]. Atoms held in shallow lattices can tunnel freely among lattice sites and form a superfluid (SF) phase. The tunneling rate is suppressed while the on-site atom-atom interaction increases in deeper lattices. This may result in a transition from a SF phase to a Mott-insulator (MI) phase at a critical lattice depth, which has been confirmed in various scalar BEC systems [4–7]. In contrast to scalar BECs, spinor BECs have unique advantages due to an additional spin degree of freedom. The predicted SF-MI phase transition is remarkably different in lattice-trapped antiferromagnetic spinor BECs; i.e., the transition may be first (second) order around the tip of each Mott lobe for an even (odd) occupation number [1,8].

Spin-mixing dynamics and phase diagrams of spinor BECs in free space, due to the interplay of the spin-dependent interaction U_2 and the quadratic Zeeman energy q_B, have been well studied using sodium [9–16] and rubidium atoms [17–20]. Known phenomena in spin-1 spinor BECs include spin population oscillations resulting from coherent interconversions among two $|F=1,m_F=0\rangle$ atoms, one $|F=1,m_F=+1\rangle$ atom, and one $|F=1,m_F=-1\rangle$ atom. Spin oscillations are harmonic except near a separatrix in phase space where the oscillation period diverges. The separatrix sets a boundary between the U_2-dominated region and the q_B-dominated region [1,15]. Richer spin dynamics are predicted in lattice-trapped spinor BECs, which allow for many immediate applications. These include constructing a novel quantum-phase-revival spectroscopy driven by a competition between U_2 and spin-independent interaction U_0, understanding quantum magnetism, and realizing massive entanglement [1,3]. However, dynamics of lattice-trapped spinor BECs remain less explored, and most of such experimental studies have been conducted in ferromagnetic ^{87}Rb spinor BECs [21–24].

In this Letter, we experimentally demonstrate that a two-dimensional (2D) optical lattice can conveniently tune spin dynamics of $F=1$ antiferromagnetic spinor BECs. We find that the properties of spinor BECs remain largely unchanged in the presence of a shallow lattice, while sufficiently deep lattices introduce some interesting changes. First, in every lattice depth u_L that supports a substantial superfluid fraction, we observe spin population oscillations after taking spinor BECs out of equilibrium at a fixed q_B. Second, we demonstrate a lattice-tuned separatrix in phase space, and explain it using lattice-enhanced spin-dependent interactions. Another remarkable result is our observation of a phase transition from a longitudinal polar (LP) phase to a broken-axisymmetry (BA) phase in steady states of spinor BECs confined by sufficiently deep lattices [25]. We find the steady states depend exponentially on q_B and sigmoidally on u_L, which agrees with our phenomenological model.

We create a BEC of 7×10^4 sodium atoms fully polarized into the $|F=1,m_F=-1\rangle$ state in a crossed optical trap similar to our previous work [14]. To adiabatically load the BEC into a 2D lattice, we decompress the optical trap to a value which minimizes intraband excitations and ensures approximately constant Thomas-Fermi radii while linearly ramping the lattice potential within $t_{\mathrm{ramp}}>40$ ms. We construct the 2D lattice in the $\hat{x}$-$\hat{y}$ horizontal plane using two linearly polarized beams which originate from a single-mode laser at $\lambda_L=1064$ nm, have a waist of $\sim$90 μm at the condensate, and are retroreflected to form standing waves. To eliminate cross interference between different beams, the two lattice beams are frequency shifted by 20 MHz with respect to each other. u_L is calibrated using Kapitza-Dirac diffraction patterns. All lattice depths studied in this Letter are kept below $15.0(8)E_R$ to avoid SF-MI phase transitions and thus maintain a sufficient superfluid fraction in our system.

Here $E_R = h^2k_L^2/(8\pi^2 M)$ is recoil energy, $k_L = 2\pi/\lambda_L$ is the lattice wave number, M is the atomic mass, and h is the Planck constant. We apply a resonant rf pulse of a proper amplitude and duration to lattice-trapped BECs for preparing an initial state with any desired combination of the three m_F states at $q_B/h = 42$ Hz, and then quench q_B to a desired value. After holding atoms for a variable time duration $t_{\rm hold}$, we abruptly switch off all lattice and trapping potentials. The fractional population of each m_F state, ρ_{m_F}, is measured with Stern-Gerlach absorption imaging after a certain time of flight $t_{\rm TOF}$. The initial ρ_0 is 0.46, the initial relative phase among the three spin states is zero, and $t_{\rm TOF}$ is 6 ms unless otherwise specified. The total magnetization $m = \rho_{+1} - \rho_{-1}$ appears to be conserved in every time evolution studied in this Letter.

In the presence of a shallow lattice of $u_L < 5E_R$, we observe spin population oscillations similar to those occurring in free space, as shown in Fig. 1. Sharp interference peaks are observed after we release BECs from the shallow lattice [see Fig. 1(a) inset], which indicates coherence and superfluid behavior in the system. As the lattice is made deeper, the separatrix position shifts to a much higher q_B, and the spin oscillations damp out more quickly (especially in the vicinity of each separatrix). These fast damped oscillations make it hard to extract oscillation periods and precisely locate each separatrix even at a moderate u_L (e.g., $4.5E_R$), as shown in Fig. 1(b). A typical anharmonic spin oscillation near a separatrix is shown in the inset in Fig. 1(b). We find our system can be understood by two models: the Bose-Hubbard (BH) model discussed in Ref. [3] for $u_L > 5E_R$, and the single-spatial mode approximation (SMA) defined in Ref. [26] for $u_L < 5E_R$. The BH model has three important terms: U_0, U_2, and the tunneling energy J among adjacent lattice sites. U_2 is proportional to the atomic density in each lattice site, and is positive (negative) in $F = 1$ ^{23}Na (^{87}Rb) BECs. In fact, $U_2/U_0 \simeq 0.04$ for our ^{23}Na system [3], and $U_2 \simeq q_B$ at each separatrix for the initial state studied in Fig. 1 [15]. The observed lattice-tuned separatrix in phase space (i.e., the separatrix position shifts with u_L) is thus mainly due to the fact that U_2 greatly increases with u_L. Figure 1(b) shows a good numerical example: U_2/h is increased from 14 Hz to 32 Hz by changing u_L from $2.5E_R$ to $4.5E_R$.

Spin oscillations completely damp out and spinor BECs reach their steady states when $t_{\rm hold}$ is long enough [see Fig. 2(a)]. Sufficiently deep lattices are found to bring some interesting changes to the steady states. Figure 2(a) demonstrates one of such changes: once u_L is sufficiently large, the steady states undergo a phase transition from a LP phase (where $\rho_0 = 1$) to a BA phase (where $0 < \rho_0 < 1$) at $m = 0$. We repeat the same measurements with only one parameter changed, i.e., by blocking the retroreflected path of each lattice beam to eliminate standing waves and construct a crossed optical dipole trap (ODT). Its resulting

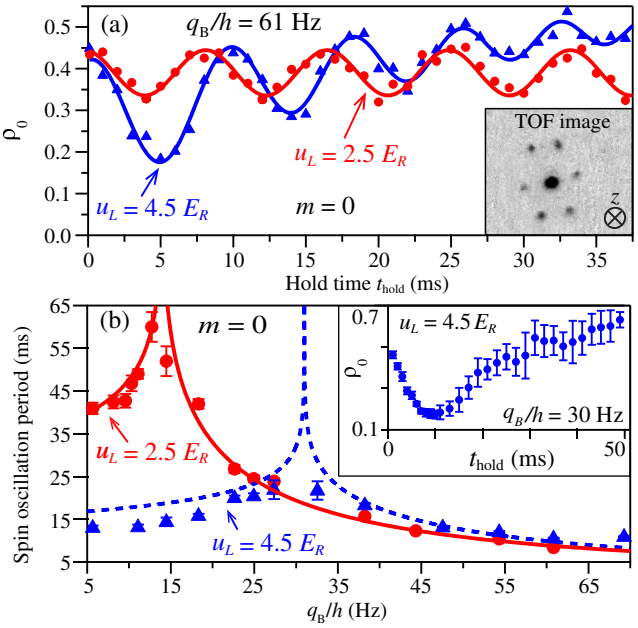

FIG. 1 (color online). (a) Time evolutions of ρ_0 when $u_L = 4.5E_R$ (triangles) and $2.5E_R$ (circles). Solid lines are sinusoidal fits to extract oscillation periods. Inset: a TOF image taken along the vertical direction (z axis) at $t_{\rm TOF} = 5$ ms. (b) Oscillation period versus q_B. Lines are fits based on SMA. Inset: time evolution of ρ_0 near a separatrix. Uncertainties are extracted from 15–20 repeated Stern-Gerlach measurements. Large uncertainties of ρ_0 near the separatrix may result from shot-to-shot fluctuations, similar to Ref. [11].

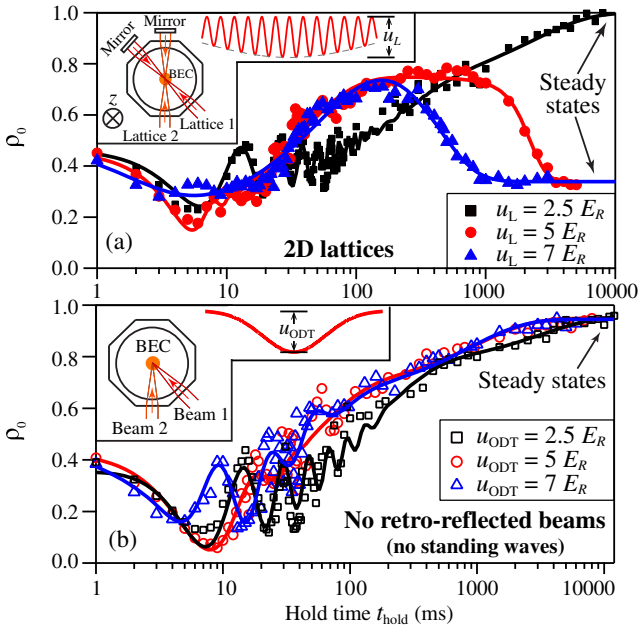

FIG. 2 (color online). (a) Time evolutions of ρ_0 at $q_B/h = 42$ Hz and $m = 0$. Inset: a schematic of our lattice setup and an illustration of the resulting lattice potential. Lines are fits to guide the eye (see Ref. [27]). (b) Similar to panel (a) except that each beam is not retroreflected.

trap depth is u_{ODT}, as illustrated in Fig. 2(b) inset. The power of every beam in Fig. 2(b) is 4 times of that in Fig. 2(a) to ensure $u_L = u_{\mathrm{ODT}}$. Our data in Fig. 2(b) show that spinor BECs at $m = 0$ always reach the LP phase when there are no standing waves. The dramatically different results shown in Figs. 2(a) and 2(b) imply a necessity to understand this LP-BA transition with lattice-modified band structures.

We then study spin oscillations and steady states within a much wider range of u_L and m. Steady states appear to depend sigmoidally on u_L at a fixed q_B, as shown in Fig. 3(a). The inset in Fig. 3(a) demonstrates another surprising result: the observed relationship between ρ_0 and m in steady states at a sufficiently large u_L is well fit by $\rho_0 = (1 - |m|)/3$, which is drastically different from a well-known mean-field prediction (i.e., $\rho_0^{D\approx 0}$ as illustrated by the black dotted line) [25]. This mean-field prediction assumes quantum depletion D is negligible, where D represents the fraction of atoms situated in non-zero momentum states. Based on Bogoliubov theory, the $D \approx 0$ assumption is correct in free space and very shallow lattices for our system [7]. We extract D from TOF images (see Fig. 3 and Ref. [28]) and confirm $D < 5\%$ at $u_L \leq 3E_R$. Note that the trapping frequency in each lattice site is much bigger than U_0/h. Our TOF images thus reflect the momentum distribution at the instant of the lattice release and enable us to directly measure D [7].

We also find that D increases with t_{hold} and u_L, and approaches one in steady states when $u_L > 10E_R$, as shown in Fig. 3(d). This lattice-enhanced quantum depletion mainly results from the lattice-flatten dispersion relation and lattice-enhanced interactions, and was originally observed in scalar BEC systems [7]. We develop one phenomenological model to incorporate the observed D and find this model can semiquantitatively describe our data without adjustable parameters, as shown in Figs. 3(a) and 4(a). In this model, the steady states are determined by a comparison between $T(\mathbf{k}, m_F = 0)$ and $T(0, m_F = \pm 1)$, where $T(\mathbf{k}, m_F)$ is the dispersion relation of the m_F state and $\mathbf{k}$ is the atom's quasimomentum. Figure 4(b) illustrates two example comparisons. Note that only the first Brillouin zone is considered, since the population in higher bands is negligible. Based on Refs. [5–7], we calculate $T(\mathbf{k}, m_F)$ as follows:

$$T(\mathbf{k}, m_F) = 4J \sum_{\alpha=x,y} \sin^2\left(\frac{\pi k_\alpha}{2k_L}\right) + E_R \frac{k_z^2}{k_L^2} + q_B m_F^2, \quad (1)$$

where a uniform density function is applied along the vertical direction without a lattice (the z axis), and J is calculated using a Wannier density function along each of the two horizontal directions with lattices. The linear Zeeman effect is ignored because it remains unchanged in coherent interconversions.

We divide $T(\mathbf{k}, m_F = 0)$ into two regions based on $T(0, m_F = \pm 1)$, i.e., set the boundary of the two regions at $\mathbf{k}_c$ which satisfies $T(\mathbf{k}_c, m_F = 0) = T(0, m_F = \pm 1)$, as marked by vertical dotted lines in Fig. 4(b). The dispersion relations are significantly flattened as u_L increases, since the predicted width of the first band is $\sim 4J$ and J exponentially reduces with u_L [6,7]. To clearly explain our model using the dispersion relations shown in Fig. 4(b), we only consider $m = 0$ and $k_y = k_z = 0$ in this paragraph. In region 1 where $0 \leq |k_x| < |\mathbf{k}_c|$, atoms in the $m_F = 0$ state always have energy smaller than those in the $m_F = \pm 1$ states. The steady states should thus be the $m_F = 0$ state (i.e., $\rho_0 = 1$), which equals $\rho_0^{D\approx 0}$. When D is big enough, atoms start to occupy region 2 where $|\mathbf{k}_c| \leq |k_x| \leq k_L$. The $m_F = 0$ atoms in region 2 are degenerate with $m_F = \pm 1$ atoms at certain other momenta. This degeneracy may account for the phenomenological relationship shown in Fig. 3(a), i.e., $\rho_0 = 1/3$ in steady states at a big u_L. Our data and the dispersion relations thus suggest that atoms in steady states may be equally distributed among the three m_F states at a big enough D.

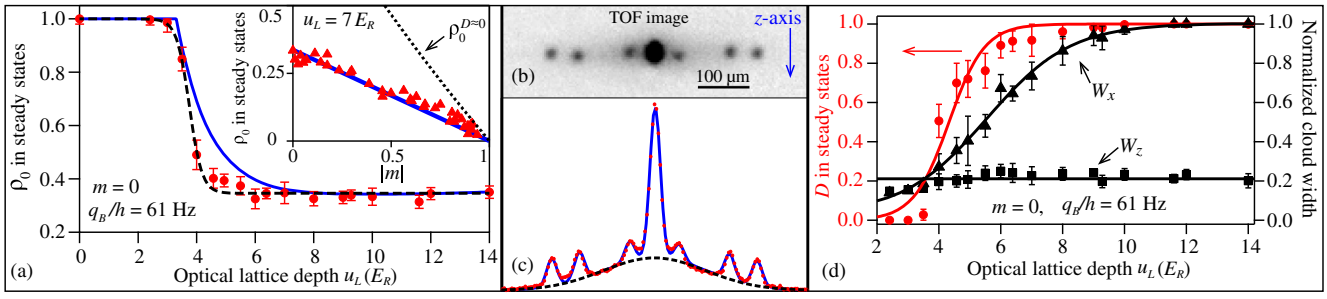

FIG. 3 (color online). (a) ρ_0 in steady states as a function of u_L (main figure) and $|m|$ (inset figure). Solid lines are predictions derived from Eq. (2). The dashed and dotted lines, respectively, represent a sigmoidal fit and $\rho_0^{D\approx 0}$ (see Ref. [25]). (b) A typical TOF image. Using method 1, the extracted D is 53% from this image (see Ref. [28]). (c) Density profile (red dotted line) of the image shown in panel (b) through all interference peaks. Using method 2 (blue solid line), the extracted D is 52.5% (see Ref. [28]). The black dashed line highlights the quantum depleted fraction. (d) W_x (triangles), W_z (squares), and D (circles) in steady states as a function of u_L. The widths are normalized by k_L. Lines are respectively sigmoid fits to W_x and D, and a linear fit to W_z.

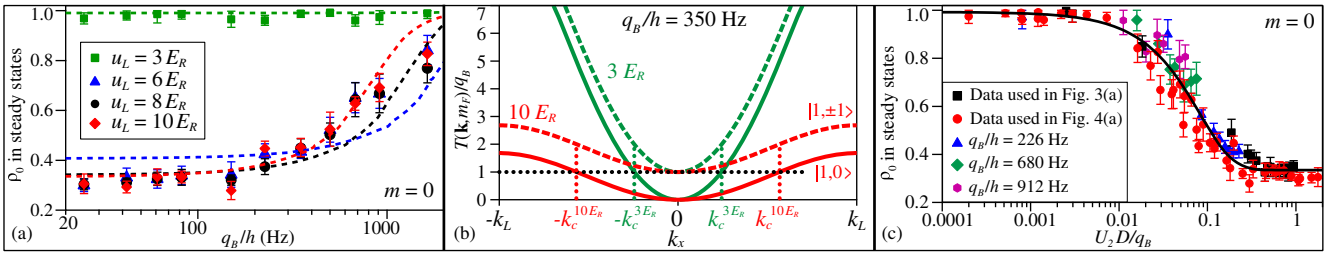

FIG. 4 (color online). (a) ρ_0 in steady states as a function of q_B. Dashed lines are predictions derived from Eq. (2). Green, blue, black, and red colors, respectively, represent results at $u_L = 3$, 6, 8, and $10E_R$. (b) Dispersion relations normalized by q_B as a function of k_x when $k_y = k_z = 0$. Solid (dashed) lines represent results of the $m_F = 0$ ($m_F = \pm 1$) states. The black horizontal dotted line marks $T(\mathbf{k}, m_F) = q_B$, and vertical dotted lines mark boundaries between region 1 and region 2 at $u_L = 3$ and $10E_R$. (c) ρ_0 in steady states versus U_2D/q_B. Black, red, blue, green, and purple colors, respectively, represent data used in Figs. 3(a) and 4(a), and additional data taken at $q_B/h = 226$, 680, and 912 Hz. The solid line is a sigmoid fit.

We can apply similar discussions and our model to all nonzero m. Thus ρ_0 in the steady states is expressed as

$$\rho_0 \approx \int_{\text{region 1}} n(\mathbf{k})\rho_0^{D\approx 0} d\mathbf{k} + \int_{\text{region 2}} n(\mathbf{k})\frac{1-|m|}{3} d\mathbf{k}. \quad (2)$$

The normalized atomic density in steady states, $n(\mathbf{k})$, is calculated by the following phenomenological formula: $n(\mathbf{k}) = (1-D)\delta_{\mathbf{k}} + D\exp[-(k_x^2/W_x^2 + k_y^2/W_y^2 + k_z^2/W_z^2)/2]/A$, where W_x and W_z are the half widths of a 2D Gaussian fit to a TOF distribution within the first Brillouin zone, $W_y = W_x$, A is a normalization factor, and δ is a Dirac-delta function [29]. Figure 3(d) shows that W_x and D sigmoidally increase with u_L, and saturate at their peak values when $u_L > 10E_R$; i.e., atoms occupy all available states and quantum depletion saturates the first Brillouin zone in a deep lattice. In contrast, W_z appears to be independent of u_L, which implies a constant system temperature.

The observed sigmoidal dependence of steady states on u_L and the exponential dependence on q_B can be explained by our model [Eq. (2)], as respectively shown in Figs. 3(a) and 4(a). Quantitative agreements between our model and data are found everywhere except in high magnetic fields where $q_B/h > 1000$ Hz, and in a lattice where $4E_R \le u_L \le 6E_R$. Limited imaging resolutions and heating induced by an extra magnetic coil in creating high q_B may both contribute to the discrepancy.

To better understand the LP-BA phase transition, we plot ρ_0 versus U_2D/q_B (a dimensionless ratio) at $m = 0$ in Fig. 4(c). Here U_2/q_B is the key factor determining the spinor dynamics in free space, D represents the lattice-induced effect, and both D and U_2 increase with the spin-independent interaction U_0. Two interesting results are found in Fig. 4(c): all 80 data points taken at very different u_L and q_B are fit by one sigmoid function; and the critical point of the LP-BA transition appears to be $U_2D/q_B \sim 0.01$. (In contrast, each predicted separatrix locates around $U_2/q_B = 1$ based on SMA and parameters studied in Fig. 4.) The LP-BA transition may thus result from a competition between q_B and the "effective" interaction U_2D; i.e., regions with strong enough interactions may prefer the BA phase. In principle, we can verify this using other methods which can efficiently tune interatomic interactions, e.g., via Feshbach resonances.

In conclusion, we have conducted the first experimental study on dynamics and the phase diagram of lattice-trapped antiferromagnetic spinor BECs. A lattice-tuned separatrix in phase space and the LP-BA phase transition in steady states have been observed. We have found that ρ_0, D, and thus the main findings of this Letter are nearly independent of t_{TOF}. We have also developed a phenomenological model that describes our data without adjustable parameters.

We thank the Army Research Office and the National Science Foundation for financial support.

*yingmei.liu@okstate.edu

[1] D. M. Stamper-Kurn and M. Ueda, Rev. Mod. Phys. **85**, 1191 (2013).
[2] Y. Kawaguchi and M. Ueda, Phys. Rep. **520**, 253 (2012).
[3] K. W. Mahmud and E. Tiesinga, Phys. Rev. A **88**, 023602 (2013).
[4] M. Greiner, O. Mandel, T. Esslinger, T. W. Hasch, and I. Bloch, Nature (London) **415**, 39 (2002).
[5] D. Jaksch, C. Bruder, J. I. Cirac, C. W. Gardiner, and P. Zoller, Phys. Rev. Lett. **81**, 3108 (1998).
[6] M. P. A. Fisher, P. B. Weichman, G. Grinstein, and D. S. Fisher, Phys. Rev. B **40**, 546 (1989).
[7] K. Xu, Y. Liu, D. E. Miller, J. K. Chin, W. Setiawan, and W. Ketterle, Phys. Rev. Lett. **96**, 180405 (2006).
[8] G. G. Batrouni, V. G. Rousseau, and R. T. Scalettar, Phys. Rev. Lett. **102**, 140402 (2009).
[9] A. T. Black, E. Gomez, L. D. Turner, S. Jung, and P. D. Lett, Phys. Rev. Lett. **99**, 070403 (2007).
[10] Y. Liu, S. Jung, S. E. Maxwell, L. D. Turner, E. Tiesinga, and P. D. Lett, Phys. Rev. Lett. **102**, 125301 (2009).
[11] Y. Liu, E. Gomez, S. E. Maxwell, L. D. Turner, E. Tiesinga, and P. D. Lett, Phys. Rev. Lett. **102**, 225301 (2009).

[12] E. M. Bookjans, A. Vinit, and C. Raman, Phys. Rev. Lett. **107**, 195306 (2011).
[13] D. Jacob, L. Shao, V. Corre, T. Zibold, L. De Sarlo, E. Mimoun, J. Dalibard, and F. Gerbier, Phys. Rev. A **86**, 061601(R) (2012).
[14] J. Jiang, L. Zhao, M. Webb, N. Jiang, H. Yang, and Y. Liu, Phys. Rev. A **88**, 033620 (2013).
[15] L. Zhao, J. Jiang, T. Tang, M. Webb, and Y. Liu, Phys. Rev. A **89**, 023608 (2014).
[16] J. Jiang, L. Zhao, M. Webb, and Y. Liu, Phys. Rev. A **90**, 023610 (2014).
[17] M.-S. Chang, Q. Qin, W. Zhang, L. You, and M. S. Chapman, Nat. Phys. **1**, 111 (2005).
[18] T. Kuwamoto, K. Araki, T. Eno, and T. Hirano, Phys. Rev. A **69**, 063604 (2004).
[19] J. Kronjäger, C. Becker, P. Navez, K. Bongs, and K. Sengstock, Phys. Rev. Lett. **97**, 110404 (2006).
[20] H. Schmaljohann, M. Erhard, J. Kronjäger, M. Kottke, S. van Staa, L. Cacciapuoti, J. J. Arlt, K. Bongs, and K. Sengstock, Phys. Rev. Lett. **92**, 040402 (2004).
[21] C. Becker, P. Soltan-Panahi, J. Kronjäger, S. Dörscher, K. Bongs, and K. Sengstock, New J. Phys. **12**, 065025 (2010).
[22] A. Widera, F. Gerbier, S. Fölling, T. Gericke, O. Mandel, and I. Bloch, Phys. Rev. Lett. **95**, 190405 (2005).
[23] P. L. Pedersen, M. Gajdacz, F. Deuretzbacher, L. Santos, C. Klempt, J. F. Sherson, A. J. Hilliard, and J. J. Arlt, Phys. Rev. A **89**, 051603(R) (2014).
[24] A. Widera, F. Gerbier, S. Fölling, T. Gericke, O. Mandel, and I. Bloch, New J. Phys. **8**, 152 (2006).
[25] Based on the mean-field theory [16], the ground states of antiferromagnetic $F = 1$ spinor BECs at a positive q_B are in one of the following three phases: (a) an antiferromagnetic phase where $\rho_0^{D\approx 0} = 0$, when $q_B < U_2(1 - \sqrt{1 - m^2})$; (b) a LP phase where $\rho_0^{D\approx 0} = 1$, when $m = 0$; (c) a BA phase where $\rho_0^{D\approx 0}$ is the root of the following equation: $1 - 2\rho_0^{D\approx 0} - [(1-2\rho_0^{D\approx 0})(1-\rho_0^{D\approx 0}) - m^2]/[\sqrt{(1-\rho_0^{D\approx 0})^2 - m^2}] = q_B/U_2$.
[26] W. Zhang, D. L. Zhou, M.-S. Chang, M. S. Chapman, and L. You, Phys. Rev. A **72**, 013602 (2005).
[27] The fitting functions used in Figs. 2(a) and 2(b) are respectively $\rho_0(t) = A_0 - A_1 e^{-t/\tau_0} - A_2/(1 + A_3 e^{-t/\tau_1}) + A_4 e^{-t/\tau_2} \sin(\omega e^{t/\tau_3} t + \phi)$ and $\rho_0(t) = A_0 - A_1 e^{-t/\tau_0} - A_2 e^{-t/\tau_1} + A_4 e^{-t/\tau_2} \sin(\omega e^{t/\tau_3} t + \phi)$, where A_0, A_1, A_2, A_3, A_4, τ_0, τ_1, τ_2, τ_3, ω and ϕ are fitting parameters.
[28] We extract N_D (the number of atoms in all nonzero momentum states) from TOF images with two fitting methods which render similar results. Method 1 is suggested by Ref. [7]: we mask off all the interference peaks, and conduct a 2D Gaussian fit to the background for extracting N_D. In method 2, we plot a density profile of a TOF image through all interference peaks, and then fit the density profile with a combination of eight Gaussian functions, i.e., one function to each interference peak, and the eighth one to the broad background for extracting N_D.
[29] The normalization factor A is an integration, $\int \exp[-(k_x^2/W_x^2 + k_y^2/W_y^2 + k_z^2/W_z^2)/2] d\mathbf{k}$, over the first Brillouin zone.